



# A Methodology for the Preliminary Design of a High-Efficiency Multistage Plasma Thruster

Nicola Puca<sup>1,2</sup> · Mario Panelli<sup>3</sup> · Francesco Battista<sup>3</sup>

Received: 30 October 2023 / Revised: 19 January 2024 / Accepted: 9 February 2024  
© The Author(s) 2024

## Abstract

Space electric propulsion represents a class of power-limited systems that utilize the interaction of electromagnetic fields with ionized inert gas propellants to generate thrust. This technology has emerged as a highly fuel-efficient and sustainable alternative to chemical propulsion systems, particularly for satellite constellations. However, the miniaturization potential of EP systems is impeded by certain limitations, necessitating the exploration of novel architectures. The high-efficiency multistage plasma thruster (HEMP-T) stands as a promising contender for stand-alone missions due to its employment of a cusped magnetic-field topology, which effectively mitigates plasma-wall interactions and enhances overall efficiency even at low thrust levels. Despite the growing interest in HEMP-Ts, there is a dearth of comprehensive and streamlined preliminary design procedures for these systems. Prior research has predominantly focused on extensive numerical analyses, neglecting the development of efficient and accessible design tools. To bridge this gap, this paper presents a novel preliminary design tool derived from integrating established analytical models available in the literature. The proposed design tool also incorporates an iterative procedure that refines geometric properties using a 2D magnetostatic solver. Through the application of this tool, a 4 mN HEMP thruster was analyzed. This finally exhibited a specific impulse of approximately 2000s and a good efficiency level of 23%. Also, the results obtained for a 10 mN application align closely with those achieved by other types of EP thrusters.

**Keywords** Electric propulsion · HEMP-T · Preliminary design · Cusped-field thrusters · Plasma thrusters

## 1 Introduction

Electric propulsion (EP) has received much attention in recent years as a worthwhile alternative to the chemical one for in-space applications on micro and nano-satellites. To date, EP systems are the first choice for micro-satellites.

The basic advantage of electric devices can be found in their high propellant exhaust speeds, which leads to high specific impulses on the one hand and a low thrust level on the other. That is mainly due to the separation of the energy source from the working fluid, that makes them far more fuel efficient when employed for long-range or long-duration missions. EP systems are, however, power-limited, since the available source on-board the spacecraft is bound to the overall mass balance of the vehicle. On the contrary, chemical propulsion systems do not require subsystems to generate energy, as this is stored in the molecular bonds of the propellant and exerted through exothermic reactions. This makes them energy-limited. These systems are therefore preferred for those types of mission where very high thrusts are required for a much shorter amount of time (e.g., launch vehicles, suborbital flights).

From an operative point of view, EP systems usually employ electrical power to ionize a propellant, produce a magnetized plasma and accelerate ions by means of the

✉ Nicola Puca  
nicola.puca@polito.it

Mario Panelli  
mario.panelli@cira.it

Francesco Battista  
francesco.battista@cira.it

<sup>1</sup> Department of Engineering, Università degli Studi della Campania Luigi Vanvitelli, Via Roma, 9, 81031 Aversa, Italy

<sup>2</sup> Present Address: Department of Mechanical and Aerospace Engineering, Politecnico di Torino, Corso Duca degli Abruzzi 24, 10129 Turin, Italy

<sup>3</sup> Centro Italiano Ricerche Aerospaziali (CIRA), Via Maiorise, 81034 Capua, CE, Italy

electric field formed between two electrodes.<sup>1</sup> The increasing need for enabling standalone micro and nano-satellites missions has stimulated great concern on emerging topics such as reliability, durability and miniaturization, and a number of novel EP concepts have come out for this purpose [1]. However, many of them proved to be inadequate for miniaturization purposes due to physical hinders. The smaller the thruster, in fact, the less efficient the plasma confinement become. Yeo et al. [2] indicated cusped field thrusters (CFTs) as one of the best candidates for down-scaling, due to their non-conventional magnetic field topology. Among these, the Thales [3] high-efficiency multi-stage plasma thruster (HEMP-T) has been considered one of the most relevant. This thruster consists of a periodically poled permanent magnets system, whose purpose is to form a cusped magnetic field topology with strong gradients towards the wall. These normally act as magnetic mirrors and reflect the charged particles back and forth, improving the electron-atom collision processes and ionization [2]. Several authors [4–6] highlighted the positive characteristics of the HEMP thruster, stressing its wide thrust range, low erosion rates [7, 8], as well as a predicted long lifetime, simple structure and cost effectiveness. Manufacturers built diverse configurations to test the performance sensitivity to some design parameters [9, 10]. A similar, even unsuccessful, variation of the HEMP-T concept was, in fact, analyzed in Boston MIT labs [11]. The so-called divergence cusped field thruster (DCFT) should have improved performance due to the conical shape of the chamber. Several operational quirks instead came up (described in [12]), resulting in no significant enhancements in the end. Another feature that developers took into account was the magnets length, as generally correlated with both the acceleration and ionization regions characteristics, as explained in [13].

Experimental campaigns about HEMP-Thrusters were carried out since the very first 2000s [14], with reported thrusts in the range of 1–43 mN and specific impulses between 1700 and 3500 s. Since the discharge chamber of these ion devices can be difficult to access with instrumentation, research has quickly shifted to numerical analyses such as the Particle-in-Cell method [15] with Monte Carlo collision models (PIC-MCC). The first successful applications of these frameworks date back to late 2000s, with contributions from [16–18]. To date, however, modeling a whole HEMP thruster is still a challenging operation because of the large lengths and time scales that need to be covered [19]. An emerging approach involves applying multi-disciplinary optimisation (MDO) techniques to let PIC simulations

directly perform on optimally designed configurations [20, 21]. These approaches have been undoubtedly rewarding for a better understanding of the internal plasma physics in HEMP-Thrusters. On the other hand, their ease of execution can be questionable when related to the need of simply getting a hint on a configuration at a preliminary design level.

To the authors' knowledge, in fact, no attempt has yet been made to provide an autonomous tool for the preliminary characterization of a HEMP-T. The purpose of this work has been, therefore, to assess a fast and manageable preliminary design methodology, capable of obtaining a quick and realistic configuration of a HEMP-Thruster without going too much into detail of the plasma characterization. As a premise, the aim of the design methodology would not be to design a HEMP-Thruster literally from scratch. The goal is to speed up the process of choosing this architecture of EP thruster with respect to another one. The overall design methodology stems from a thrust requirement as the main input parameter. An early stage of initialization then takes place using data from some few available prototype examples in the literature. The early characterization of the thruster is refined through the application of basic analytical plasma models, while the geometric parameters are fixed through the performing of 2D magnetostatic analyses. The tool was used to pre-design a 4 mN HEMP thruster, since this was set as the basic requirement for enabling novel missions such as LUMIO [22] and M-Argo [23]. The paper verified that a realistic first guess 2D prototype can be obtained and be in line with the expected operative parameters. Feasibility was also tested for the characterization of 10 mN thruster example.

A description of the HEMP-T concept is given in the next paragraph. Then, the following Sect. 2 outlines the whole design methodology with a specific focus on the analytical framework description. Two mathematical models are outlined and compared to those existing in literature. The sizing tool is then specifically applied for two cases in Sect. 3. Conclusions and future developments for this work are presented in Sect. 4.

## 1.1 HEMP-Thruster Concept

A schematic view of a HEMP thruster is depicted in Fig. 1. A cylindrical chamber with a set of pairwise opposite polarity permanent magnets (PPMs) are employed to form the typical cusped magnetic field topology. At cusps, a radial B-field starts from the chamber wall, causing the electrons to continuously oscillate along the field lines due to the magnetic mirrors. This is generally responsible of reducing the phenomenon of wall erosion. A rear mounted anode also serves as a neutral gas injector (e.g., for Xenon or Krypton), while outside the discharge chamber a hollow

<sup>1</sup> That is not the case of electrothermal thrusters (arcjets, resistojets) which normally heat the propellant and rely upon thermal dynamics to propel the whole system.

Fig. 1 Schematic of a HEMP thruster

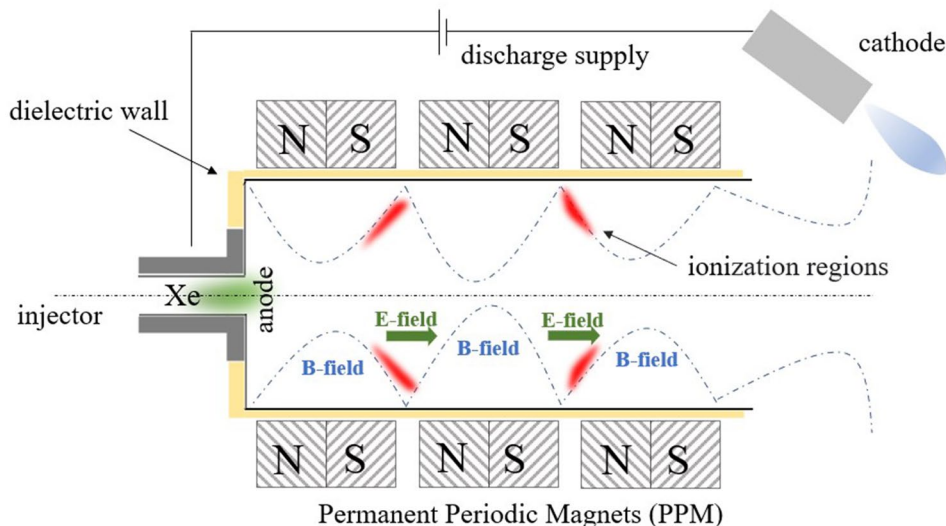
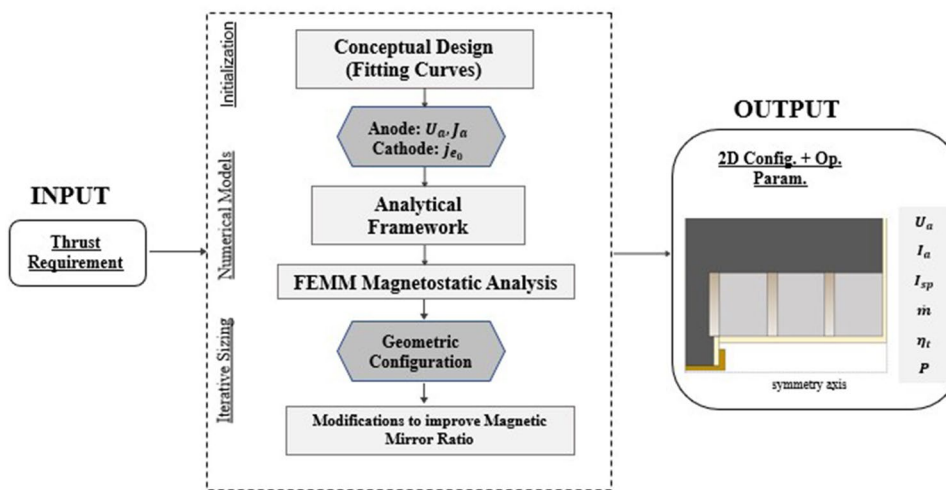


Fig. 2 General workflow of the HEMP-T design methodology

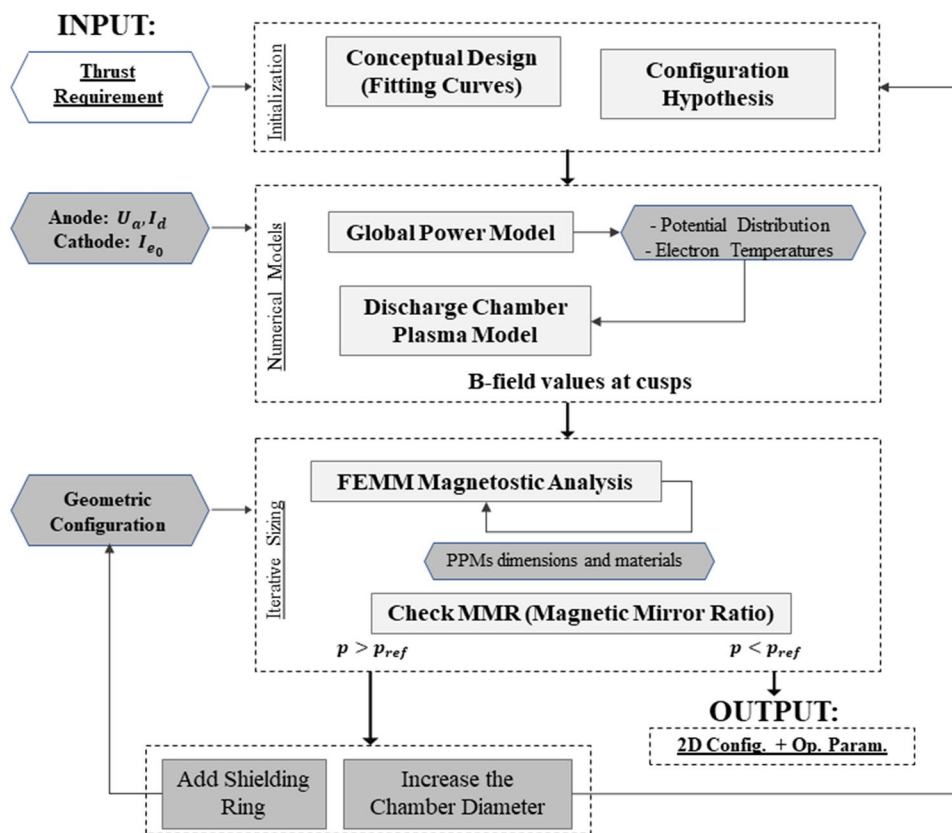


neutralizing cathode is located. Electrons are accelerated towards the chamber from that, and then trapped into the magnetic mirrors. The potential difference ranges typically from 300 V up to 6000 V [5] between the electrodes. The energies of the impinging ions are usually not high enough to cause significant sputtering, so this results in very low thermal losses [2]. The ions are accelerated out of the thruster [24]. This acceleration takes place almost entirely at the thruster due to the rapid drop of electric potential and electron density. Also, the lack of physical grids prevents the thruster from experiencing erosion problems. Like Hall effect thrusters (HETs), the discharge chamber is usually coated with a dielectric material (boron nitride is a common choice). An additional material with high magnetic permeability (pure iron, Mu-Metal) is instead employed for the group of ring-shaped separators which are placed between the magnets [2].

## 2 Materials and Methods

A comprehensive overview of the methodology is presented in Fig. 2, while the complete procedure is outlined in Fig. 3. Starting from the thrust mission requirement, a basic configuration can be retrieved by means of interpolating data from some existent prototypes in literature. These also serve to determine the initial electrode conditions for the analytical section that follows. A mathematical model is then derived based on power balances such as in Ref. [25]. This provides (a) the electric potential distribution and (b) the electron temperature profile along the chamber. These functions are provided as piece-wise quantities, as the model involves dividing the thruster into a finite number of stages, called magnetic cells. A subsequent discharge chamber plasma model is employed to search for an estimation of the magnetic field scalar magnitudes at the cusps.

Fig. 3 Detailed workflow of the HEMP-T design methodology



Once the overall operative characterization is reached, an iterative numerical procedure with FEMM (Finite Element Method Magnetic) can be applied. This will consist of continuously varying the magnets’ thickness and materials to make the B-field analytical values overlap with the simulated ones. The final refinement deals instead with measuring the magnetic mirror ratios and keep them within predetermined bounds. These quantities can be defined as the ratios between the B-field magnitude at cusps and between them. Generally speaking, when the B-field gradient decreases, the magnetic mirror effects become weaker and the probability of electrons reaching the wall at the cusps increases. That probability will be adopted as a design variable through the final refinement. The analytic expression that is commonly employed [25] for its computation is given in Eq. (12) with respect to a generic cell. The value  $p$  depends on the magnetic gradient  $x = B_m/B_{c_m}$ , where  $B_m$  and  $B_{c_m}$  stand for the magnitude of B at cell centers and at cusps, respectively, with  $m$  the  $m$ -th cusp. The assumption typically is that only those electrons with a velocity direction within an acceptance angle  $\alpha_a$ , with respect to the magnetic B-field, can reach the cusp. Assuming the generic cell  $j$ ,  $\alpha_a \leq \arcsin \sqrt{B_{m_j}/B_{c_j}}$ . Therefore, Eq. (12) follows from Ref. [25]:

$$p_j = \frac{1}{2} \int_0^{\alpha_a} \sin \theta \, d\theta \tag{1}$$

$$\theta = \arcsin \sqrt{\frac{B_m}{B_{c_m}}} \tag{2}$$

As the terms  $p_j$  are correlated with magnetic mirror ratios, the final goal of the design procedure will also be to keep these probabilities as low as possible and comparable with literature values. To do this, some possible design modifications have been investigated. These were all oriented at lowering the magnetic field strength in the plasma bulk or increasing it at walls, so as to raise the B-field gradient along the axis. The possible solutions that were examined were to consider a larger chamber diameter or to employ a thin magnetic ring [26] near the exit section. Actually, these solutions could be applied at the same time, too. The preliminary design procedure stopping condition is then satisfied once all the probabilities  $p$  are low enough to agree with literature expectations.

This section introduces the analytical framework which was developed to characterize the thruster. The hypothesis

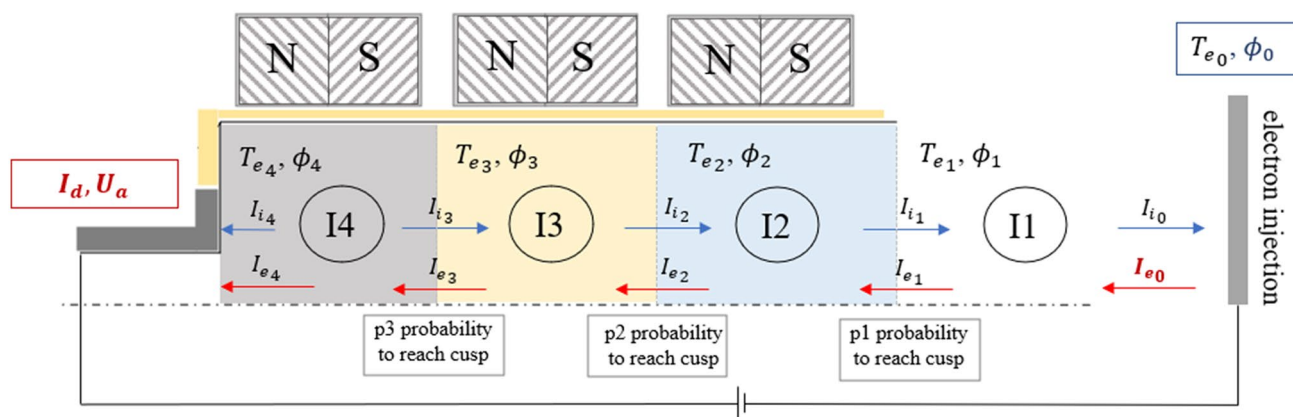


Fig. 4 Simplified circuit and power balance model of the HEMP-T numerical model, adapted from Kornfeld [25]

and modifications to the models have been thought to make them specifically suited for HEMP-Thrusters.

### 2.1 Numerical Power Balance Model

A simplified power balance description of a HEMP thruster based on plasma fluid theory has been chosen and reviewed from Ref. [25]. This Section will discuss the basic assumptions behind this model. Then, an extended equations framework will be proposed and included in the preliminary design methodology.

Given the voltage and current conditions at the electrodes as inputs, the model from Kornfeld in Ref. [25] yields a set of nonlinear constrained coupled equations. These are mainly based on writing down the local balance equations for energy and currents. Their number will in fact depend on how many magnetic cells can be defined. Since some previous works [13] verified this is the configuration to get major pluses (such as stronger electron confinement ability, or lower losses), the overall design methodology within this paper will assume three stages of permanent magnets, resulting into four separate cells. Moreover, Xenon was selected as propellant according to almost all the HEMP-Thrusters prototypes available in the literature. The propellant selection affects the model by modifying empirical estimates for global energy transfers in the system. These are given by the relative fraction of the gained electron power transferred to excitation (CE) and the fractions for ionization (CI) and thermalization (CT). These parameters were fixed according to the assumptions of the model by Kornfeld.

A schematic of the thruster model is sketched in Fig. 4, which also highlights the aforementioned division into a given number of cells, here indexed with  $j = 1 \dots 4$ . The model typically considers the external region standing in front of the cathode as the first magnetic cell, even if not bounded with walls. Constant local properties are assumed within these regions, so that a piece-wise distribution for

potential and electron temperature will be obtained as final output. The overall analytical framework can be found in Ref. [25], and consists of 28-equations with 28 unknowns. Apart from cell voltages  $\phi_j$ , or temperatures  $T_e$ , the output list also includes the ionization source currents  $I_j$ , and the electron/ion currents flowing through each magnetic cell. The complete list of physical assumptions can be accessed in the original research paper. However, some of them can be recalled briefly: (i) the potential boundary condition at the cathode is supposed to be  $\phi_0 = 0$  V; (ii) the remaining conditions at electrodes (potentials and currents) are assumed to be known in advance as main input parameters for the entire model; (iii) electrons can hit the dielectric wall at the cusps, and that requests an identical ion current for charge compensation; this condition determines the so-called self-consistently adjusting cusp potentials  $\phi_{c_j}$ ; (iv) at each cusp the sum of electron and ion currents should be zero, as the wall surface is supposed to be of a dielectric; (v) charge and energy conservation laws are valid for each magnetic cell.

Clearly, some limitations stand for this model; its application, in fact, should be entrusted just to introductory design phases, as done in [20, 21]. Also, the model cannot directly estimate the necessary magnetic field magnitudes within the thruster. Furthermore, the model does not take into account neither the influence of neutral gas density distribution, nor the ionization efficiency, the doubly charged ions, and the details of the ion beam structure. These gaps were roughly filled through the adoption of another plasma model for the discharge chamber, which will be discussed in Sect. 2.2.

The first balance equation employed in the model is Eq. 3, which shows the overall power conservation inside the thruster. On the left-hand side, the delivered electric power will be the product between the anode voltage  $U_a$  and the discharge current  $I_d$ . Both of them are input parameters to the model. This product has to match with the sum of the

ion beam power  $P_b$ , the frozen losses and all the thermal dissipation at anode and the respective magnetic cusps, on the right-hand side. The term IL represents the ionization losses, while EL, CL and AL are the excitation, cusp and anode losses, respectively.

$$U_a I_d = P_b + IL + EL + CL + AL \tag{3}$$

A power balance is then carried out also for each of the four magnetic cells, resulting in four more equations (Eq. (4) with  $j = 1, \dots, 4$ ). The received electron power from the generic downstream cell is expressed on the left-hand side, while a sum of direct cusp losses, thermalized power, ionization and excitation losses can be found on the right-hand one. The term IE is the ionization energy for Xenon and is assumed to be 12.1 eV.

$$\begin{aligned} & I_{e_{j-1}}(1-p_j)(q\phi_j - q\phi_{j-1} + T_{e_{j-1}}) \\ & + I_{e_{j-1}}p_j(q\phi_{c_j} - q\phi_{j-1} + T_{e_{j-1}}) \\ & = I_{e_{j-1}}p_j(q\phi_{c_1} - q\phi_{j-1} + T_{e_{j-1}}) \\ & + (I_{e_{j-1}}(1-p_j) + I_j)T_{e_j} \\ & + I_jIE + I_{e_{j-1}}(1-p_j)CE(q\phi_j - q\phi_{j-1} + T_{e_{j-1}}) \end{aligned} \tag{4}$$

Current balances at the interfaces between cusps (Eq. (5)) and at the cathode (Eq. (6)) are then added to the model.

$$I_d = I_{e_j} + I_j \text{ for } j = 1, \dots, 4 \tag{5}$$

$$I_d = I_{e_0} + I_{i_0} \tag{6}$$

Then, three boundary interface conditions (zero currents at three dielectric cusps) are expressed with Eq. (7). The term  $p_j$  is the probability of electrons to reach the  $j$ -th cusp surface.

$$I_{e_{j-1}}p_j = I_{i_{c_j}} \text{ for } j = 1, 2, 3 \tag{7}$$

At the cathode, the model assumes a space charge limited emission which can be described by a selected perveance  $p_0$ . This results in  $I_{e_0} = p_0\phi_1^{3/2}$ . A value for the perveance was selected according to Ref. [25]. To close the analytical 28-equations framework, the following definition relationships were added.

$$I_{e_j} = I_{e_{j-1}}(1-p_j) + I_j \text{ for } j = 1, \dots, 3 \tag{8}$$

$$I_j = I_{e_{j-1}}(1-p_j)CI\left(\frac{\phi_j - \phi_{j-1} + T_{e_{j-1}}}{IE}\right) \text{ for } j = 1, \dots, 4 \tag{9}$$

$$I_{i_{j-1}} = I_{i_j} + I_j - I_{i_{c_j}} \text{ for } j = 1, \dots, 3 \tag{10}$$

$$I_{i_3} = I_4 - |I_{i_4}| \tag{11}$$

$$T_{e_j} = \frac{CTI_{e_{j-1}}(1-p_j)(\phi_j - \phi_{j-1} + T_{e_{j-1}})}{I_{e_j}} \text{ for } j = 2, \dots, 4 \tag{12}$$

A set of plausible physical restrictions was defined for this model. These actually turned into a set of mathematical constraints for the equations system. The electron temperatures must be greater than zero, and the potentials at the cusps are bound to be lower than their corresponding values at the cells centers. Major details can be found in the reference. Almost all the restrictions, however, can be regarded as linear inequality constraints, except for the non-linear one in Eq. (13).

$$|I_{i_3}| > |I_{i_4}| \tag{13}$$

Within this paper, a larger model with 33 equations was employed to make up for some shortcomings found in the application of the original. Specifically, a first estimate for the terms  $p_j$  was missing, so that an extension of the main equations problem was employed considering them as unknowns. The probabilities  $p_j$  are, in fact, typically employed to quantify the effectiveness of the electrons trapping within the magnetic mirrors. A higher probability means a worse effect of the magnetic mirror and vice versa. Since the operative definition given in Eq. (12) turned out to be hardly usable, the selected way to compute them analytically was through the definitions derived from Matthias [4] in Eq. (14).

$$p_j = 1 - \frac{I_{e_j} - I_j}{I_{e_{j+1}}}, \quad j = 1, 2, 3 \tag{14}$$

Within this formula, the incoming  $I_{e_j}$  and outgoing  $I_{e_{j+1}}$  electron current are compared. The remaining term  $I_j$  stands for the ionization source currents generated inside each cell. With these, three more equations were added to the original 28-dimensional system; however, the new unknowns would be four due to the remaining term  $p_4$  that should be computed. Therefore, to let the equations and unknowns number match, the electron current  $I_{e_0}$  emitted from the cathode was converted to an input parameter. Doing so, the modified model will require the choice of a cathode with its emission current before being solved. To that point, the 31-equations model obtained so far was further modified with two more equations aimed at turning the non-linear constraint in Eq. (13) into a linear one. The final version to operate on was a

33-equations system, with also new constraints to be put into account.

An optimization problem-based strategy was followed for the model solving. Two possible algorithms were selected and compared:

- (i) a Genetic Algorithm (GA), which should minimize the objective function in Eq. (15), built as a weighted<sup>2</sup> sum of squares involving the equations written in their implicit form  $F_i(x_i) = 0, \quad i = 1, \dots, n$ ;

$$f_{\text{obj}} = \text{norm} \left( \begin{bmatrix} Q_1 & 0 & 0 & 0 \\ 0 & Q_2 & 0 & 0 \\ 0 & 0 & \ddots & 0 \\ 0 & 0 & 0 & Q_n \end{bmatrix} \begin{Bmatrix} F_1(\mathbf{x}) \\ \dots \\ F_n(\mathbf{x}) \end{Bmatrix} \right) \quad (15)$$

- (ii) the MATLAB built-in nonlinear programming solver |fminconl, which requires to reformulate the problem into the minimization of a constant objective function subject to a set of nonlinear equality constraints which coincide with the equations themselves.

The GA works on a population using a set of biologically inspired operators to let it evolve in time and reduce to a single optimal individual. A population is a set of points in the design space, which for the application in this section will coincide with a set of 33-dimensional feasible vectors.

Apart from the algorithm parameters, the initial population of solutions has a significant influence on the quality of the results, but also on the convergence speed of the algorithm. The initial population is normally generated with random variables picked up between predetermined lower and upper bounds. As a consequence, this may lead to solutions of poor quality. Concerning the resolution of the numerical power balance model of this section, the initial random population for the genetic algorithm was pre-conditioned with the addition of the two already known individuals from Ref. [25]. This modification was intended to make the final result converge to a solution vector with more plausible and physically valid quantities.

The DM9.2 and DM10 prototypes from Ref. [25] were used as a benchmark to prove the capabilities of the customized numerical model. Table 1 outlines the outputs and compare them with the data sheets. A GA solver was employed. To let the remaining part of the preliminary design tool work reliably, the best comparison should be ensured for what

<sup>2</sup> All weights are grouped into the coefficients  $Q_i$ , whose role is to help managing the different orders of magnitude among the type of variables involved. Greater weights should apply to those balance or definition equations aimed at determining currents and probabilities, as these typically are the variables with the narrowest interval of variability.

**Table 1** 33-equations model validation using the solutions from [25]

	DM9.2	DM9.2*	DM10	DM10*
$\phi_1$ [V]	14.02	14.1	12.27	12.3
$\phi_2$ [V]	979.15	1000	979.26	979
$\phi_3$ [V]	998.90	1000	998.88	999
$\phi_4$ [V]	1000	1000	1000	1000
$\phi_{c_1}$ [V]	12.2	8.1	12.2	12.2
$\phi_{c_2}$ [V]	978.99	960	978.99	979
$\phi_{c_3}$ [V]	978.99	965	978.99	979
$T_{e_1}$ [eV]	7.88	8.9	7.89	7.8
$T_{e_2}$ [eV]	99.52	100.1	99.84	99.8
$T_{e_3}$ [eV]	47.99	43.1	48.04	48.1
$T_{e_4}$ [eV]	26	23.5	26.02	26.2
$I_1$ [A]	- 0.0644	0.008	- 0.0294	0.006
$I_2$ [A]	0.5235	0.543	0.5066	0.473
$I_3$ [A]	0.3180	0.310	0.3182	0.361
$I_4$ [A]	0.2212	0.157	0.2214	0.229
$I_{e_1}$ [A]	0.2528	0.107	0.2267	0.090
$I_{e_2}$ [A]	0.6165	0.637	0.5964	0.557
$I_{e_3}$ [A]	0.7788	0.845	0.7786	0.882
$I_{e_4}$ [A]	0.9432	1.002	1	1.111
$I_{i_0}$ [A]	0.8160	0.894	0.8931	0.914
$I_{i_1}$ [A]	0.8994	0.893	0.9050	0.910
$I_{i_2}$ [A]	0.3835	0.363	0.4036	0.442
$I_{i_3}$ [A]	0.2212	0.155	0.2214	0.118
$I_{i_4}$ [A]	0	- 0.002	0	- 0.111
$I_{i_{c_1}}$ [A]	0.0484	0.007	0.0159	0.002
$I_{i_{c_2}}$ [A]	0.0835	0.013	0.0709	0.006
$I_{i_{c_3}}$ [A]	0.1556	0.102	0.1360	0.037
$p_1$ [-]	0.49	0.06	0.57	0.024
$p_2$ [-]	0.63	0.119	0.60	0.064
$p_3$ [-]	0.25	0.160	0.23	0.066
$p_4$ [-]	6.1e-13	0.254	7.6e-14	0.092

Columns with \* stand for the solutions taken from the original model

concerns potentials and electron temperatures, as these are the quantities that will directly affect the following stages of the design process. The corresponding was generally good for these parameters, even if the overlapping vanishes and the error increases for some terms, such as the probabilities  $p$  or some ion/electron currents. Therefore, this validation phase proved that the proposed analytic pathway for the estimation of  $p_j$  in Eq. (12) cannot be adopted as a trustworthy solution.

Similar conclusions may be drawn when replicating this validation case with the use of the |fminconl function. A different validation example is instead proposed in Table 2. This has been reported to highlight the difference between GA and |fminconl when applied to other thrusters rather than the ones suggested in Ref. [25]. The numerical 33-dimensional model was, in fact, fed with the operative

**Table 2** 33-equations model validation using thrusters from the literature: comparison between the use of fmincon and GA functions

	NG $\mu$ HEMP-T		DM3a	
	Fmincon	GA	Fmincon	GA
$\phi_1$ [V]	6.099	15.82	13.82	19.86
$\phi_2$ [V]	649.46	699.10	486.81	499.8
$\phi_3$ [V]	661.31	699.93	486.96	499.93
$\phi_4$ [V]	700	700	500	500
$T_{e_1}$ [eV]	17.61	16.23	19.52	17.55
$T_{e_2}$ [eV]	59.19	100.54	64.93	100.2
$T_{e_3}$ [eV]	42.58	41.42	31.89	43.28
$T_{e_4}$ [eV]	33.85	24.17	24.03	23.66

parameters of two distinct HEMP-Thrusters and solved with GA and |fmincon|, respectively. Not all the parameters are known from datasheets to make a fully realistic validation. The table is indeed reporting just two kind of outputs, potentials and temperatures. The GA solver ended up being affected by the given initial population. The values for electron temperatures, in fact, are found to be insensitive to the change in input conditions and still similar to the ones recorded for the thrusters in Table 1. This is pretty much evident when referring, for example, to the  $T_{e_3}$  temperature, that still remains high even if the NG -  $\mu$ HEMP-T and the DM3a have lower powers. On the contrary, using the less time-expensive and flexible |fmincon| the results can feel the effects of different operating conditions. That is the reason why MATLAB's |fmincon| was finally chosen and applied for the numerical model resolution.

### 2.2 Discharge Chamber Plasma Model

Quantitative B-field values can be determined using another analytical model, derived by making some modifications to the one provided by Goebel [27] for ring-cusp

ion thrusters. Clearly, some important differences must be taken into account to let this model fit with the HEMP-T concept, such as considering (i) higher discharge voltages, (ii) a dielectric wall in the chamber, (iii) higher electron temperatures, (iv) a different loss mechanism (wall losses are enhanced and estimated from the sheath potentials), (v) the presence of an external neutralizing cathode, (vi) the absence of grids. Also, it should be pointed out that the B-field lines of HEMP-Thrusters converge to form cusps between the magnets and not at their centers.

The original model proposed by Goebel assumes uniform plasma properties in the whole chamber. On the contrary, for HEMP-Thrusters, different average energy levels (electron temperature) can be defined for each magnetic cell. Given their absence, each property for the grids should be dropped out from the equations. Also, the grid area  $A_g$  will be replaced simply by the exit circular cross section of the thruster. Apart from the different nature of boundary walls and magnets sizes, the HEMP-T device could be broken down into the same elements as a ring-cusp thruster. Figure 5 reproduces the basic layout of the Goebel's model. Two species of electrons can be defined. Mono-energetic electrons with  $I_{e_0}$  current are assumed to be emitted from the external hollow cathode orifice into the chamber. These are called *primaries*. Plasma electrons are instead placed inside the discharge chamber and tend to make many Coulomb collisions with each other. Therefore, the model assumes they can usually be characterized by a Maxwellian distribution. Primaries can be lost both through collisions with the neutral gas, or ballistically to the walls. The result will be in any case a thermal equilibrium condition into the chamber (thermalization) with the plasma electrons.

Some fraction of the primary electrons is lost directly to the wall at the magnetic cusps ( $I_{e_c}$ ). Coming to plasma electrons, instead, a predominant loss typically occurs on the wall cusps ( $I_{p_c}$ ), while just a small fraction goes across the transverse magnetic field between the cusps. Figure 5

**Fig. 5** Schematic of a HEMP-T showing particle flows, adapted from [27]

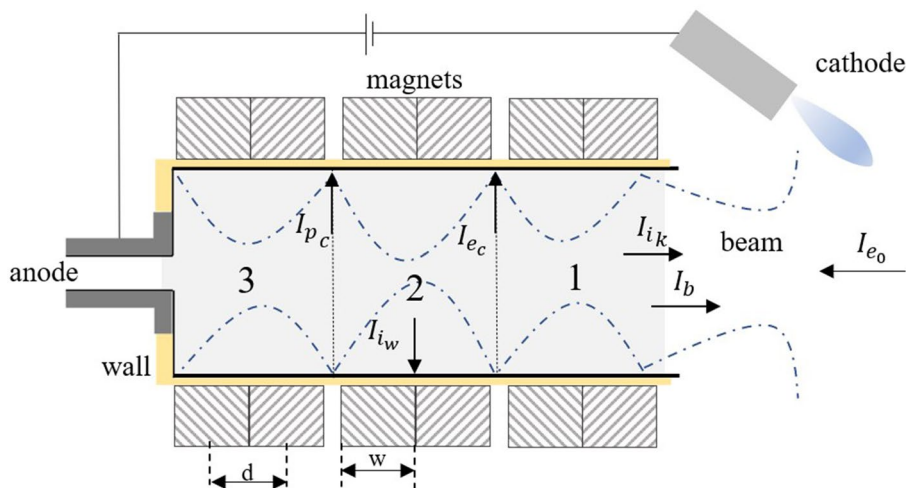




**Table 3** Main equations for the discharge chamber plasma model, adapted from Ref. [27] to fit with the HEMP thruster application

Equations	Symbols
1.1 $I_{e_c} = n_p q v_p A_p$ $A_p = 2r_p L_c$ $v_p = \sqrt{\frac{2q(\Delta U + \phi_s)}{m}}$ $n_p = \frac{I_{e_0} v_0 A_g \eta_m}{4\Omega_j \sigma v_p I_b (1 - \eta_m)}$	<b>Main</b> — $n_p$ : primaries density, $v_p$ : velocity of primaries, $A_p$ : primaries loss area <b>Secondary</b> — $r_p$ : Larmor radius for primaries, $L_c$ : cusp length, $\sigma$ : total inelastic collision section for primaries, $\Omega_j$ : magnetic cell geometric volume
1.2 $I_{p_c} = \frac{1}{4} \left( \frac{8kT_e}{\pi m} \right)^{1/2} q n_e A_a e^{\left( -\frac{q\phi_s}{kT_e} \right)}$ $A_a = \sqrt{r_e r_i} L_c$ $n_e = \frac{I_b}{q A_c \sqrt{\frac{2m_e q v_0}{M}}}$	<b>Main</b> — $T_e$ : electron temperature in the magnetic cell, $n_e$ : plasma electrons density, $A_a$ : hybrid loss area <b>Secondary</b> — $r_e$ : Larmor radius for plasma electrons, $r_i$ : Larmor radius for ions, $A_c$ : thruster cross-section
1.3 $I_{i_w} = \frac{1}{2} n_i q \sqrt{\frac{kT_e}{M}} A_{as} f_c$ $A_{as} = \pi D L_j$	<b>Main</b> — $A_{as}$ : wall surface exposed to the plasma, $f_c$ : ion confinement factor, $n_i$ : ion density <b>Secondary</b> — $D$ : thruster diameter, $L_j$ : cell geometric length

also reports the ion current transverse to the magnetic field between the cusps to the wall ( $I_{i_w}$ ), and the ion current to the cathode ( $I_{i_k}$ ). Unlike GITs, the voltage in the chamber is high enough to trigger double ionization phenomena with the formation of the so-called *secondary* electrons.

As mentioned, this model is mainly aimed at the determination of the B-field magnitude values at cusps,  $B_{c_j}$ , with  $j = 1, 2, 3$ . These will then be compared with those obtained from numerical simulations to select the magnets configuration that is most capable of recreating conditions similar to the analytical results. Overall, the model reduces to writing the conservation of particles for each magnetic cell, as in Eq. (16).

$$I_{p_c} = I_d + I_{i_w} - I_{e_c} \tag{16}$$

The term  $I_d$  indicates the discharge current measured in the discharge plasma supply. Its determination will be discussed in the next section. This current balance can be made explicit and solved for the B-field magnitude values at cusps. Table 3 can be accessed to review the main equations involved in the derivation of  $B_{c_j}$ . Each formula should be applied 3 times, as 3 are the magnetic cells inside the discharge chamber.

**Equation Block 1.1:** Since  $r_p$  inversely depends on the magnetic field strength B, a strong magnetic field will minimize the contact area of electrons with the wall. Assuming the electron as a classical particle of mass  $m$  and charge  $q$ , the velocity  $v_p$  can be computed by invoking the conservation of energy. This will result in having  $v_p$  expressed as a function of the potential drops through each cell,  $\Delta U = \phi_{j+1} - \phi_j$ . Concerning  $\phi_s$ , instead, this stands for the sheath potential. Sheaths are transitional regions of plasma with large potential drops and strong electric fields, which typically create a bridge between the bulk of the plasma and the walls of the vessel in which it is contained. Given

the high voltages that are typically reached in the chamber, HEMP-Thrusters can trigger double ionization phenomena like HETs. Therefore, concerning the plasma sheath analytical formulation, the discharge chamber plasma model will employ the framework proposed for Hall-effect thrusters in Goebel’s textbook [27, Chapter 7].

To make the density  $n_p$  for primary electrons explicit, the velocity of neutrals should be computed, too. Assuming the wall temperature  $T_w$ <sup>3</sup> to be constant throughout the whole thruster, the neutrals will have the same velocity in each magnetic cell. This is up to Eq. (17), where  $M$  is the mass of a Xenon particle and  $k$  the Boltzmann’s constant:

$$v_0 = \sqrt{\frac{8kT_w}{\pi M}} \tag{17}$$

The equation for  $n_p$  does involve two more terms. The beam current  $I_b$  and the mass utilization efficiency  $\eta_m$  can be known in advance within the early conceptual design phase (curve fitting). Their evaluation will be clear in the next sections, when the entire preliminary design methodology will be applied for two assumed thrust requirements.

**Equation Block 1.2:** This block is aimed at computing the flux of plasma electrons that is lost at the wall cusps, namely  $I_{p_c}$ . Computing this current will require to express the electron number density  $n_e$ . This is assumed equal to ions’ according to the quasi neutrality hypothesis for plasma. Specifically, the computation of  $n_e$  refers to the highest temperature region in the channel (Chapter 7, Ref.

<sup>3</sup> The neutral gas atoms collide several times with the wall before being lost, so that the neutral gas can be assumed to have the average temperature of the thruster body in contact with the plasma. A good approximation can be 200–300 °C according to Goebel’s reference. The model employed  $T_w = 250$  °C.

[27]). Plasma electrons are almost exclusively lost at the magnetic cusps. That is true even for some ions, so that an hybrid "loss" area can be defined at the cusps,  $A_a$ . Again, like for  $A_p$ , this term involve an inverse proportionality with the magnetic field  $B$  at cusps that the model wants to determine in the end. The equation for  $A_a$  has been revised with respect to the original model to let it fit with the physical characteristics of the HEMP thruster.

Much literature has been in fact produced in the last decades to derive scaling laws for particle loss areas, or loss widths [28, 29]. Hershkowitz et al. [28] were among the firsts to find these in the order of 4 times the hybrid gyroradius. However, to know how the leak width scales is a very questionable topic, and a unique answer does not exist. Although distinct groups of authors showed experiments that proved the dependence with the hybrid gyroradius, some different theories were spread out, stating that the dependence was to be sought just by looking at the ion Larmor radius. The study from Knorr and Merlino [30] proved that a decrease of high energy primary electrons could drastically increase the leak width above the known values. With this in mind, since the energy levels in the HEMP-Thrusters are very high, the proportionality coefficient was supposed to be lower and simply equal to 1.

**Equation Block 1.3:** As for GITs and HETs, ions are considered not to be affected by magnetization when considering HEMP-Thrusters. While the ion currents to the hybrid cusp areas can be neglected, the loss areas are significantly higher between the cusps, and the ion current going towards the wall  $I_w$  has to be computed. The so-called confinement factor  $f_c$  (between 0 and 1) takes into account the influence of the reduced transverse electron drift speed on the ion motion. This is linked to the transverse B-field arising between cusps. The reduction in the ion velocity flowing radially to the wall for the situation of a transverse magnetic field was better analyzed in Goebel's textbook. The term  $A_{as}$ , finally, represents the wall surface exposed to the plasma for the specific cell, which is simply the lateral surface area of the cylindrical cell. Since magnetic cells have been considered equal in length, this parameter can be defined once.

The ion confinement factor is supposed to be unknown for this model. An iterative procedure, therefore, was employed for its selection. The requirement to fulfill was to choose the one that makes the power balance equations satisfied for each cell. This requires to determine 3 different  $f_c$  values. To do so, local power balances were added to the set of equations. Equation (18) computes the input power for the generic magnetic cell  $j$ . The term in brackets stands for the voltage that electrons gain as they pass from one cell to another. The formula was adapted to the HEMP-T case by introducing the relative potential jump  $\Delta U$ . The term

$V_p$  (potential drop in the plasma) can be computed for the generic magnetic cell as  $V_p = kTe/2q$ .

$$P_{IN_j} = I_{e_0}(\Delta U + V_p + \phi_s) \quad (18)$$

The power leaving the generic cell  $j$  takes into account either the ions flowing to the wall or to the anode, and the primary and plasma electrons flowing to the wall. Some contributions arising for GITs, however, were neglected when adapting to the case of HEMP-Thrusters, such as those depending on grid currents. The overall relation will be:

$$P_{OUT_j} = I_p U^+ + I^* U^* + (I_{j+1} + I_w)(V_p + \phi_s) + I_{p_c} \epsilon_e + I_c(\Delta U + V_p + \phi_s) \quad (19)$$

While the term  $I_w$  is still an unknown into the problem, the term  $I_{j+1}$  can be directly taken from the outputs of the numerical power balance model in 2.1. Then,  $I_p$  is the total number of ions produced in the discharge,  $U^+$  is the ionization potential of the propellant gas,  $I^*$  is the number of excited ions produced in the discharge chamber and  $U^*$  is the excitation energy. More details on these parameters can be found in Ref. [27]. The plasma electron energy lost to the wall, instead, can be derived from Appendix C of [27] as  $\epsilon_e = 2kT_e/q + \phi_s$ .

## 3 Results and Discussion

### 3.1 Curve Fitting Approach

The literature was analyzed to set up a dataset based on the existing HEMP-T prototypes in the range of few newtons of thrust. The aim was to employ the dataset to elicit specific correlation laws between the main operative parameters, just by feeding a group of fitting curves with the thrust requirement as input value. Since the thrust must be considered as fixed for the application in this paper, other parameters were gathered instead for the thrusters in the dataset, including the anode power  $P$ , the overall efficiency  $\eta_t$ , and the discharge current  $I_d$ . Additional characteristics were instead introduced in the form of geometric measurements, as their definition is intricately linked to the HEMP-T architecture. Comparatively, HEMP-Thrusters exhibit a simpler construction geometry in contrast to other EP systems. Consequently, only a few basic geometric quantities like the chamber diameter and length will govern critical performance aspects. An additional parameter to collect in the dataset was the outer diameter, OD. While the former parameters are self-explanatory, the latter has been specifically defined in the manuscript as the aggregate of the cross-sectional area with the wall and magnet thicknesses. Table 4 shows the limited set of the examples that were retrieved from the references

**Table 4** Dataset of HEMP-Thrusters retrieved from the literature

HEMP-Thrusters Dataset	
HEMP-T 3050 DM9-1 [32]	$F_t = 50$ mN
HEMP-T EV0 [31]	$F_t = 17.7$ mN, $F_t = 32$ mN
NG $\mu$ HEMPT [5]	$F_t = 3.236$ mN
mini NG $\mu$ HEMPT [5]	$F_t = 0.086$ mN
DCFT (MIT) [11]	$F_t = 13.4$ mN
DCFT (Stanford) [33]	$F_t = 4.9$ mN
Hu Prototype [34]	$F_t = 9.5$ mN
CFT-20 [35]	$F_t = 18$ mN

about low thrust HEMP-Thrusters. A single nominal design point was chosen for each thruster, except for the HEMP-T EV0 [31], whose characterization was very much detailed in the related research work with several design points. As one can recognize, the list includes also some of the DCFT architectures, which differ for having a conical rather than straight discharge chamber. Coming to the diameter datum, for that case, just the smaller one was considered to make data almost consistent one to the other. This will not be an issue for the rest of the sizing methodology. This design stage, in fact, just will serve to infer a realistic mock-up of the thruster as the basis for all the subsequent analytical steps. The diameter itself, for instance, will be even changed further on according to the B-field configuration to obtain.

The plots depicted in Fig. 6 show the fitting curves that were generated. Since the primary objective of the design procedure is to generate an initial design for a HEMP-Thruster based solely on a thrust requirement, a considerable portion of the curves were created to investigate the relationship between each of the other parameters and the thrust itself. The reader may notice varying the number of data points on different graphs. This variation arises from missing or unreliable information pertaining to certain thrusters within the dataset. These latent data points were symbolized by a green cross. Also, the reader can see that the interval on the  $x$ -axis might not remain the same for each of the fitting curves, as it mostly depends on which is the thrust interval for which a good polynomial law is valid. Considering this, the assessment of the overall design tool feasibility in this phase was established to meet a thrust requirement of up to 10 mN.

Anyway, the small database derived in Table 4 cannot independently guarantee a robust and standalone procedure. Some important aspects would in fact be still missing for a complete characterization, such as a better characterization of the B-field inside the chamber. While this fitting curves-based approach might be adequate for outlining an initial rough design of the thruster, its primary function is to identify crucial parameters necessary for executing the subsequent analytical processes. Both the power balance model

and the discharge chamber plasma model were precisely developed with the aim of enriching the characterization of the thruster as well as refining some of the quantities that the initial conceptual phase of the design cannot handle in a robust manner. Through these models, as a matter of fact, a refinement will be made of the initial design with a slight deviation from the influence of the existing thrusters in the dataset.

Employing the data fitting-based approach of this section also proved to be beneficial in delving deeper into the understanding of the physics within the chamber of a HEMP-Thruster. Concerning the length  $L$ , for instance, the observed increasing-decreasing pattern with respect to the efficiency implies several considerations. On one hand, a longer discharge channel typically extends the ionization region, which tends to enhance propellant utilization, thereby resulting into a better efficiency. An excessively long chamber, in contrast, may lead to a critical increase in ion wall losses, potentially causing a detrimental effect on the efficiency.

Some minor geometrical choices were frozen from the beginning, as the result of estimations taken from visual schematics of existing thrusters. The parameters involved into this were for example the dielectric thickness, the injector diameter, or all the anode dimensions. The following assumptions were also made for the completion of the design, inspired by the common choices in the literature: (a) the anode consists of a long conducting stainless steel rod terminated by a prominent rounded tip (b) the anode is assisted by a boron nitride riser allowing the magnetic mirror ratio to be controlled through its axial position relative to the B-field lines; (c) a distance thin plate made of Mu-Metal acts as a separator between the opposite poled magnets; (d) the thruster half-width has been selected to satisfy the dimensional requirement of 1U CubeSat ( $100 \times 100 \times 100$  mm); (e) housing material is 316 Stainless Steel.

### 3.2 4 mN Case Application

The HEMP-T preliminary design methodology outlined in this paper was tested for a 4 mN thrust requirement. At first, the early conceptual design phase with fitting curves returned an initial estimation of both the anode conditions. Once the global power and the discharge current are known, determining the corresponding voltage can be done straightforward by definition. Similarly, some more quantities can be derived from the estimations provided with the curves in Fig. 6. These are summarized in Table 5.

The estimated voltage and current were  $U_a = 666$  V and  $I_d = 0.24$  A, respectively. Then, the numerical model in Sect. 2.1 was applied. Concerning the electron current  $I_{e0}$

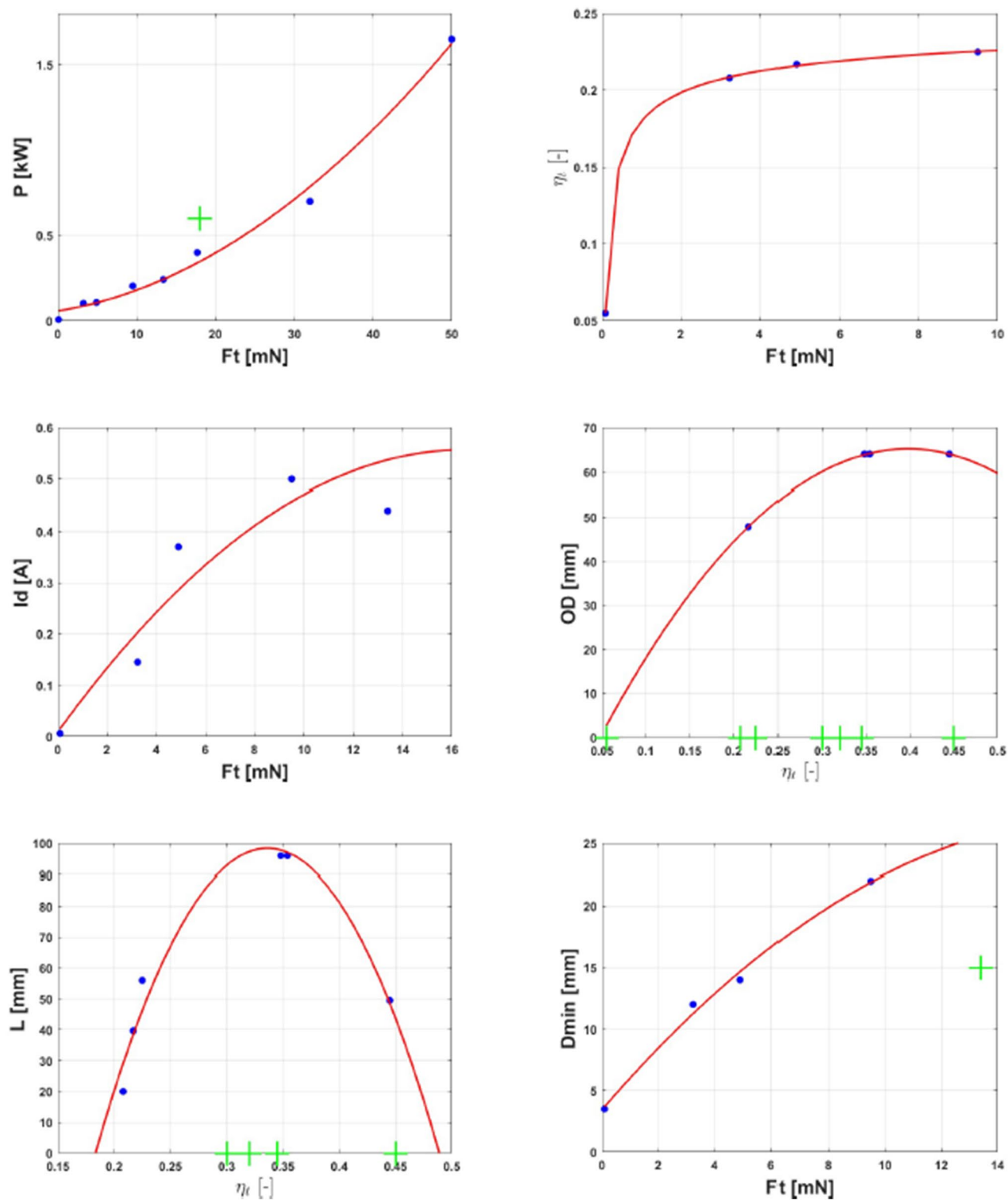


**Fig. 6** Fitting curves. black dots indicate data where available, while the green crosses testify an unavailability

coming from the cathode, this was set by assumption to the same value that held for the DM9.2 prototype in [25]. The most important solution parameters are provided in Table 6.

As expected from literature [5, 25] potentials are almost the same for each cell except the exit one, where the drop is more evident and responsible for the final acceleration

**Table 5** Additional operational parameters obtained through estimates from the curve fitting stage of the design

Inferred operative parameters	
Anode voltage [V]	$U_a = P/I_d$
Mass flow rate [kg/s]	$\dot{m} = F_t/2\eta_t P$
Specific impulse [s]	$I_{sp} = F_t/\dot{m}g_0$

**Table 6** Numerical model solutions for a 4mN HEMP-Thruster with  $U_a = 666$  V,  $I_d = 0.24$  A,  $I_{e_0} = 0.16$  A

Global power model solutions			
$\phi_1$ [V]	18.76	$T_{e_1}$ [eV]	22.91
$\phi_2$ [V]	633.62	$T_{e_2}$ [eV]	36.27
$\phi_3$ [V]	645.04	$T_{e_3}$ [eV]	27.97
$\phi_4$ [V]	666.66	$T_{e_4}$ [eV]	26.01

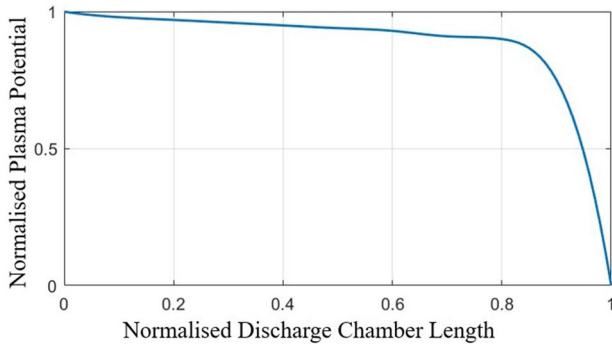


**Fig. 7** Qualitative plasma potential inside the cavity of a HEMP-T, adapted from Ref. [5]

of ions (Fig. 7). Temperatures rise in the middle regions<sup>4</sup> of the thruster, where the main ionization occurs.

These outputs were then subject to post-processing calculations aiming at the characterization of the plume. To this end, beam divergence angle was assumed to be constant as in Ref. [20]. Instead, multiple ion species were considered together with the double ionization effect, so that a correction factor  $\alpha_c = 0.9$  from [20] was introduced in the simplified divergence efficiency Eq. (20). The significance of the angle  $\theta_d$  is connected to the geometrical opening of the ion plume at the exit of the thruster. The

<sup>4</sup> Apart from the improvement in the ionization zones, the characteristic high temperature values for HEMP-Thrusters can be associated to another physical reason. Part of the high energy electrons, which are not reflected by the magnetic bottle, hit the wall and lead to secondary electron emission. The secondary electrons are accelerated towards the channel plasma thanks to the potential drop at the sheath, leading to an additional increase of the electron temperature in the cusp region [4].

value was assumed to be  $60^\circ$  as in the paper of Fahey et al. [20].

$$\eta_d = \alpha_c \frac{1 + \cos(\theta_d)}{2} \tag{20}$$

Then, the voltage efficiency,  $\eta_v$ , was simply derived as the ratio between the potential drop through the chamber  $V_b$  and the anode voltage  $U_a$ . The mass utilization efficiency  $\eta_m$  instead reports how many neutral particles really get ionized inside the thruster; its calculation comes from inverting the specific impulse definition in Eq. 21 from Ref. [5].

$$I_{sp} = \frac{F_t}{g_0 \dot{m}} = \frac{\eta_d \eta_m}{g_0} \sqrt{\frac{2qV_b}{M}} \tag{21}$$

Specifically, the mass utilization efficiency can be defined as the ratio of the beam current to the maximum current obtainable from the flow rate under the assumption of singly charged ions, being this determined as  $I_n = q\dot{m}/M$ . With this in mind, the mass utilization efficiency calculation becomes more explicit in Eq. (22). The beam current, finally, is computed in Eq. (23), showing a direct relation with the mass flow rate. Both singly and doubly ionized particle currents are typically taken into account with the definition of  $I_b$ , as it is shown by the presence of the  $\alpha_c$  coefficient.

$$\eta_m = \frac{\dot{M}}{\dot{m}} = \frac{I_b M}{q \dot{m}} = \frac{I_b}{I_n} \tag{22}$$

$$I_b = \frac{\eta_m q \dot{m}}{\alpha_c M} \tag{23}$$

Similar to what has been seen for the voltage, the ratio between the beam current  $I_b$  and the anode current was set to define an approximation of the beam efficiency,  $\eta_b$ . More realistic values would otherwise require experimental campaigns and the use of appropriate instrumentation. Bearing all this in mind, the global efficiency value was updated and refined using a more detailed formulation [5, 20] which typically splits it into a combined product of all the sub efficiencies which have been defined so far (Eq. (24)).

$$\eta_t = \eta_d^2 \eta_b \eta_v \eta_m \tag{24}$$

The scaling procedure continues, then, through the application of the discharge chamber plasma model discussed in Sect. 2.2. This process enables the estimation of the magnetic field magnitudes at the cusps, resulting in the acquisition of three desired values, since three are the intermediate regions between one set of magnets and the other. These quantities were deemed compatible with the findings reported in the literature (e.g., Hey [5]) concerning new generation HEMP-Thrusters.

The next step of the methodology involved fine-tuning the geometric properties of the magnets. The purpose has been to replicate the obtained B-field magnitudes within the contour plots of a numerical simulation executed with FEMM [36]. With other words, the B-field values that were obtained using the discharge chamber plasma model served as a guide for sizing the magnets. A first-guess value for their thickness can be already derived by difference, actually, just by knowing the outer diameter, the cross dimension of the chamber and the thermal insulation layer, as reported in Sect. 3.1. The refinement strategy outlined at this stage of the procedure, instead, was conceived as a more specific tool for determining the magnets dimensions. Essentially, it involved executing multiple magnetostatic simulations, each one considering a different thickness of the magnets, denoted as  $r_{mag}$ . A range of potential magnets widths was therefore selected for investigation, within the assumption of initially keeping the diameter of the chamber and the wall thickness unchanged. Along with the geometric quantity, the refinement strategy also took into account the possibility of varying the material to employ, as this can affect the magnetic induction properties. Just the default material libraries in FEMM were tested, such as some different types of Samarium–Cobalt (SmCo) or Neodymium (Ne) magnets. To save time, an external controlling script written in MATLAB [36] was employed. This script facilitated the execution of multiple simulations at one time through a single input command. This way, the need to manually set up the specific geometry each time was avoided. The parameters under investigation were systematically varied across a predefined range of feasible values for the analysis, so that each configuration to be tested consisted into a pair of material and thickness values. The final choice was based on the comparison of the simulated B-field punctual magnitudes with those derived from the discharge chamber plasma model. Before assessing the final magnet configuration, however, an additional evaluation regarding the operational temperature of the magnets was integrated in the MATLAB routine. A rough estimation can be obtained using the Stefan–Boltzmann relation referred to the emission properties of the boron nitride dielectric walls. This is reported in Eq. (25), where the parameter  $\sigma_B$  is the Stefan–Boltzmann constant, and  $\epsilon$  indicates the emission coefficient for boron nitride.

$$P = \sigma_B \epsilon S (T^4 - T_{env}^4) \tag{25}$$

Regarding temperatures,  $T$  represents the unknown temperature, while  $T_{env}$  was designated as 300 K (which is typical for laboratory applications). The symbol  $S$  finally denotes the emission surface, which is assumed to be the lateral surface area of the cylindrical discharge chamber. The unknown temperature must be less than the Curie temperature for the selected material, on pain of excluding the current

**Table 7** Design and working parameters of the final chosen 4mN HEMPT configuration

	Symbol	Value
Specific impulse	$I_{sp}$	1907 s
Anode power	$P$	160 W
Anode efficiency	$\eta_t$	0.2338
Anode voltage	$U_a$	666.67 V
Discharge current	$I_d$	0.24 A
Mass flow rate	$\dot{m}$	0.21 kg/s
Channel diameter	$D$	20 mm
Outer diameter	$OD$	65 mm
Anode diameter	$D_a$	16 mm
Anode axial length	$l_a$	12 mm
Channel length	$L$	54.3 mm
Injector diameter	$D_j$	1.5 mm
Magnet width	$r_{mag}$	21.5 mm
Magnet material		SmCo 24
Additional ring width	$w_r$	2 mm
Ring distance from exit	$d_r$	5 mm
B-field at exit cusp	$B_{c_1}$	0.58 T
B-field at middle cusp	$B_{c_2}$	0.59 T
B-field at anode cusp	$B_{c_3}$	0.89 T
$B_{m_1} / B_{c_1}$		0.58
$B_{m_2} / B_{c_2}$		0.59
$B_{m_3} / B_{c_3}$		0.73

configuration and searching for the one which is immediately after. The Curie point, or Curie Temperature, is in fact the temperature at which a magnetic material undergoes a sharp change in its magnetic properties.

The final evaluation before confirming the magnets configuration involved assessing the magnetic mirror ratio for each cell. By definition, this ratio must be less than unity, or whichever as small as possible to maximize the impact of the magnetic mirrors. An indicative threshold value was selected to automate the design procedure, allowing it to stop once all three magnetic ratios become feasible. Upon the fulfillment of this condition, the preliminary design methodology will have identified the definitive configuration.

Some strategies were implemented to modify the design at this point, aiming either to reduce the B-field within the chamber or to increase that on the cusps. As the introduction of a small geometric divergence in the chamber would invalidate a substantial part of the analytical framework, two alternative modifications were implemented. One of these is about adding a specific aluminum/iron magnetic shielding ring near the thruster’s exit to enhance ionization. This choice was supported by evidence in the literature [26]. At the same time, increasing the diameter of the chamber turned

**Fig. 8** 4 mN HEMP-T final configuration with the additional magnet ring near the exit

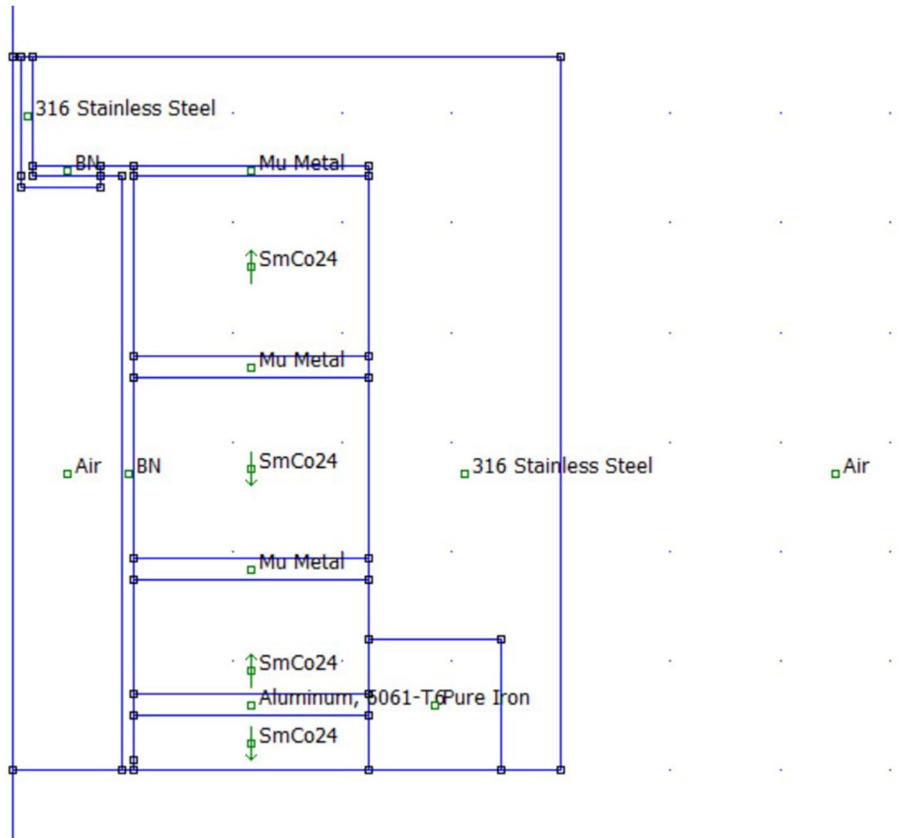


**Fig. 9** 4 mN HEMP-T final configuration, 2D density plot

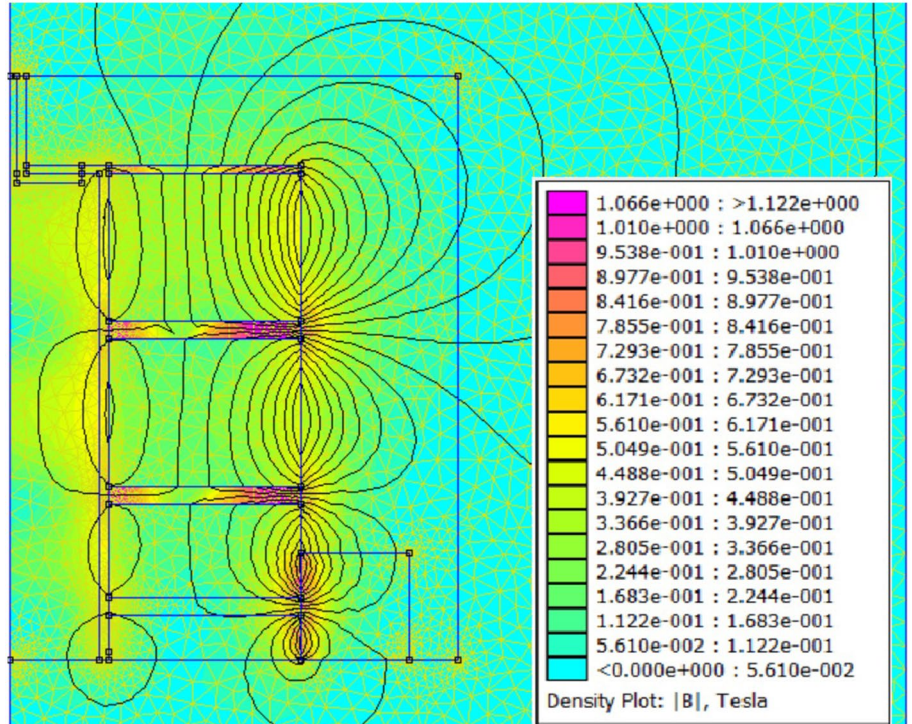


**Table 8** Design and working parameters for a 10 mN HEMP-T configuration

	Symbol	Value
Specific impulse	$I_{sp}$	829 s
Anode power	$P$	180 W
Anode efficiency	$\eta_t$	0.226
Anode voltage	$U_a$	381.5 V
Discharge current	$I_d$	0.47 A
Channel diameter	$D$	22.5 mm
Outer diameter	$OD$	49.5 mm
Anode diameter	$D_a$	18.5 mm
Channel length	$L$	47.3 mm
Magnet width	$r_{mag}$	2.7 mm
Magnet material		SmCo 32
B-field at exit cusp	$B_{c_1}$	0.21 T
B-field at middle cusp	$B_{c_2}$	0.37 T
B-field at anode cusp	$B_{c_3}$	0.30 T
$B_{m_1}/B_{c_1}$		0.42
$B_{m_2}/B_{c_2}$		0.37
$B_{m_3}/B_{c_3}$		0.44

out useful for reducing the B-field within the chamber. A smaller diameter would indeed necessitate an higher magnetic field strength to achieve a predetermined performance, and vice versa. Both of these solutions were incorporated into the final design after undergoing numerical validation using FEMM. The final configuration was obtained and summarized in Table 7 with its main performance and working parameters.

Figure 8 represents the thruster 2D scheme, giving particular focus on the material labels associated to each portion of the architecture. The results of the magnetostatic analysis are instead shown in Fig. 9 through a common FEMM-based density plot.

### 3.3 10 mN Case Application

The design methodology was also applied again for a different thrust requirement, namely 10 mN. A slightly higher anode power was found, as well as a decrease in specific impulse. The global efficiency instead did not change that much with respect to the 4 mN case. The thrust change seemed to influence the anode conditions, since the voltage dropped down to almost 400 V while current was doubled up to near 0.5 A. The other parameters were obtained exactly in the same way as the previous sections have described. No further modifications were necessary to improve magnetic mirror ratios. All the information gathered for the 10 mN sizing application was summarized in Table 8.

Data is consistent with what reported by Conversano [37] concerning a magnetic shielded Hall effect thruster

with almost an equal power. According to these measurement campaigns, indeed, a complete characterization of the MaSMi-40 thruster was achieved at 330 W nominal point, resulting in a thrust of 13 mN at an anode efficiency of 24%. This Hall effect device was employing a fully shielding magnetic field topology to produce a dramatic increase in the useful life of the channel. Doing a partial comparison between that and the 10 mN HEMP-T data sheet in Table 8, efficiency values are seen almost to overlap each other. This could be a numerical proof for indicating at a first glance the HEMP-T as a deserving alternative to HETs, even to some of their magnetically shielded configurations. Clearly, these two thrusters should be compared also for what concerns durability and erosion rates. Only detailed analyses could detect which is the best. In fact, efficiency is not always the only thing that matters; in the case of the BHT-200, for example, which is a 3 cm Hall thruster capable of 11.4 mN of thrust at an anode efficiency of 42%, operational life is very limited [37].

## 4 Conclusion

This study presented a comprehensive methodology for the preliminary design of medium-to-low power HEMP-Thrusters. By providing a thrust requirement as the primary input, the methodology successfully delivered the operational characterization of the thruster as the final output. The developed sizing tool demonstrated its feasibility for thrust requirements ranging from 1 to 10 mN. The pre-design phase involved a fitting curves-based approach to establish correlation laws for determining some key operational parameters. Subsequently, a customized analytical equations model was employed to calculate temperatures and potentials within the chamber. Additionally, an analytical model facilitated the computation of punctual magnetic field values within the thruster. The final step involved geometric refinement for the magnets. The proposed methodology proved capable of offering an autonomous, self-regulating, and reliable design procedure, rendering it a valuable alternative to experimental and numerical analyses, particularly at the conceptual design level. The preliminary design of 4 and 10 mN HEMP-Thrusters was presented and discussed, demonstrating configurations that align reasonably well with existing literature. However, the tool's applicability is constrained by the assumptions made for the plasma analytical models. Validation posed challenges due to the absence of fully characterized HEMP-T prototypes in the open literature. While partial validation was achieved for the Kornfeld's modified numerical model, further proof of feasibility is required for the discharge chamber plasma model. From a simulation perspective, conducting detailed thermal and plasma



analyses would enhance result cross-verification. These areas of improvement and validation should be addressed in future research on this topic. The clues provided herein will guide forthcoming endeavors aimed at refining and expanding the knowledge in HEMP-Thrusters.

**Acknowledgements** The authors would like to thank prof. E. Martelli (University of Campania, L. Vanvitelli, currently at Politecnico di Torino), who entrusted his graduated student (NP) to CIRA space propulsion laboratory, giving him the possibility to contribute to this study.

**Author Contributions** Not applicable.

**Funding** Open access funding provided by Politecnico di Torino within the CRUI-CARE Agreement. This research was funded by the Italian research program in aerospace, PRORA (*Programma Operativo Ricerche Aerospaziali*) entrusted by MIUR (*Ministero dell'Istruzione, Ministero dell'Università e della Ricerca*).

**Availability of Data and Materials** Available.

**Code Availability** Available.

## Declarations

**Conflict of interest** The authors declare that they have no known competing financial interests or personal relationships that could have appeared to influence the work reported in this paper.

**Ethics approval** Not applicable.

**Consent to participate** Not applicable.

**Consent for publication** Agreed.

**Open Access** This article is licensed under a Creative Commons Attribution 4.0 International License, which permits use, sharing, adaptation, distribution and reproduction in any medium or format, as long as you give appropriate credit to the original author(s) and the source, provide a link to the Creative Commons licence, and indicate if changes were made. The images or other third party material in this article are included in the article's Creative Commons licence, unless indicated otherwise in a credit line to the material. If material is not included in the article's Creative Commons licence and your intended use is not permitted by statutory regulation or exceeds the permitted use, you will need to obtain permission directly from the copyright holder. To view a copy of this licence, visit <http://creativecommons.org/licenses/by/4.0/>.

## References

- Lev, D., Myers, R.M., Lemmer, K.M., Kolbeck, J., Koizumi, H., Polzin, K.: The technological and commercial expansion of electric propulsion. *Acta Astron.* **159**, 213–227 (2019). <https://doi.org/10.1016/j.actaastro.2019.03.058>
- Yeo, S.H., Ogawa, H., Kahnfeld, D., Schneider, R.: Miniaturization perspectives of electrostatic propulsion for small spacecraft platforms. *Prog. Aerosp. Sci.* (2021). <https://doi.org/10.1016/j.paerosci.2021.100742>
- Koch, N., Harmann, H.P., Kornfeld, G.: Development and test status of the Thales high efficiency multistage plasma thruster family. In: Paper presented at the 29th International Electric Propulsion Conference, Princeton University, October 31–November 4 2005 (2005)
- Matthias, P., Kahnfeld, D., Schneider, R., Yeo, S.H., Ogawa, H.: Particle-in-cell simulation of an optimized high-efficiency multistage plasma thruster. *Contrib. Plasma Phys.* (2019). <https://doi.org/10.1002/ctpp.201900028>
- Hey, F.G. (ed.): *Micro Newton Thruster Development, Direct Thrust Measurements and Thruster Downscaling*. Springer, Friedrichshafen (2017)
- Keller, A.: Feasibility of a down-scaled HEMP thruster. PhD thesis, Justus-Liebig-University Gießen I. Physikalisches Institut (2013)
- Koch, N., Schirra, M., Weis, S., Lazurenko, A., Van Reijen, B., Haderspeck, J., Genovese, A., Holtmann, P., Schneider, R., Matyash, K., Kalentyev, O.: The HEMPT concept—a survey on theoretical considerations and experimental evidences. In: Paper presented at the 32th International Electric Propulsion Conference, Wiesbaden, Germany, September 11–15 2011 (2011)
- Gildea, S.R., Matlock, T.S., Martinez-Sanchez, M., Hargus, W.A.: Erosion measurements in a low-power cusped-field plasma thruster. *J. Propuls. Power* **29**, 906–918 (2013). <https://doi.org/10.2514/1.B34607>
- Ma, C., Liu, H., Hu, Y., Yu, D., Chen, P., Sun, G., Zhao, Y.: Experimental study on a variable magnet length cusped field thruster. *Vacuum* **115**, 101–107 (2015). <https://doi.org/10.1016/j.vacuum.2015.02.007>
- Liu, H., Zeng, M., Yu, D., Huang, H.: Study of channel length effect on low power HEMP thruster. *Vacuum* (2019). <https://doi.org/10.1016/j.vacuum.2019.02.035>
- Courtney, D.G., Lozano, P., Martinez-Sanchez, M.: Continued investigation of diverging cusped field thruster. In: Paper presented at the 44th AIAA/ASME/SAE/ASEE Joint Propulsion Conference and Exhibit, Hartford, July 21–23 2008 (2008)
- Matlock, T.S.: An exploration of prominent cusped-field thruster phenomena: the hollow conical plume and anode current bifurcation. PhD thesis, Massachusetts Institute of Technology (2012)
- Hu, P., Yu, D., Yan, S.: Magnet stage optimization of 5 kW multi-cusped field thruster. *Plasma Sci. Technol.* (2020). <https://doi.org/10.1088/2058-6272/aba680>
- Kornfeld, G., Koch, N., Coustou, G.: First test results of the HEMP thruster concept. In: Paper Presented at the 28th International Electric Propulsion Conference, Toulouse, March 17–21 2003 (2003)
- Tskhakaya, D., Matyash, K., Schneider, R., Taccogna, F.: The particle-in-cell method. *Contrib. Plasma Phys.* **47**, 563–594 (2007). <https://doi.org/10.1002/ctpp.200710072>
- Matyash, K., Kalentev, O., Schneider, R., Taccogna, F., Koch, N., Schirra, M.: Kinetic simulation of the stationary HEMP thruster including the near-field plume region. In: Paper Presented at the 31st International Electric Propulsion Conference, University of Michigan, Ann Arbor, Michigan, USA, September 20–24 2009 (2009)
- Matyash, K., Schneider, R., Mutzke, A., Kalentev, O., Taccogna, F., Koch, N., Schirra, M.: Kinetic simulations of SPT and HEMP thrusters including the near-field plume region. *IEEE Trans. Plasma Sci.* **38**, 2274–2280 (2010). <https://doi.org/10.1109/TPS.2010.2056936>
- Brandt, T., Braxmaier, C., Trottenberg, T., Jansen, F., Kersten, H., Hey, F.G., Johann, U.: Simulation for an improvement of a down-scaled HEMP thruster. In: Paper Presented at the Joint Conference of the 30th International Symposium on Space Technology and Science, 34th International Electric Propulsion Conference and 6th Nano-satellite Symposium, Hyogo-Kobe, Japan, 2015 (2015)
- Kahnfeld, D., Duras, J., Matthias, P.: Numerical modeling of high efficiency multistage plasma thrusters for space applications.

- Rev. Mod. Plasma Phys. **3**, 1–43 (2019). <https://doi.org/10.1007/s41614-019-0030-4>
20. Fahey, T., Muffatti, A., Ogawa, H.: High fidelity multi-objective design optimization of a downscaled cusped field thruster. *Aerospace* (2017). <https://doi.org/10.3390/aerospace4040055>
  21. Yeo, S. H., Ogawa, H.: Investigation of influence of magnet thickness on performance of cusped field thruster via multi-objective design optimization. In: Paper Presented at the 2018 Asia-Pacific International Symposium on Aerospace Technology (APISAT), Chengdu, China, October 16–18 2018 (2018)
  22. Space Missions Engineering Laboratory.: Lunar meteoroid impact observer. <https://home.aero.polimi.it/space/?Projects:LUMIO>. Accessed: 2023-04-05
  23. M-Argo.: Journey of a suitcase-sized asteroid explorer. [https://www.esa.int/Enabling\\_Support/Space\\_Engineering\\_Technology/Shaping\\_the\\_Future/M-Argo\\_Journey\\_of\\_a\\_suitcase-sized\\_asteroid\\_explorer](https://www.esa.int/Enabling_Support/Space_Engineering_Technology/Shaping_the_Future/M-Argo_Journey_of_a_suitcase-sized_asteroid_explorer). Accessed: 2023-04-05
  24. Hu, P., Liu, H., Gao, Y., Mao, W., Yu, D.: An experimental study of the effect of magnet length on the performance of a multi-cusped field thruster. *J. Phys. D Appl. Phys.* (2016). <https://doi.org/10.1088/0022-3727/49/28/285201>
  25. Kornfeld, G., Koch, N., Harmann, H.P.: Physics and evolution of HEMP-Thrusters. In: Paper Presented at the 30th International Electric Propulsion Conference, Florence, Italy, September 17–20 2007 (2007)
  26. Hu, P., Liu, H., Mao, W., Yu, D., Gao, Y.: The effects of magnetic field in plume region on the performance of multi-cusped field thruster. *Phys. Plasmas* (2015). <https://doi.org/10.1063/1.4932077>
  27. Goebel, D., Katz, I.: *Fundamentals of Electric Propulsion Ion and Hall Thrusters*, JPL Space Science and Technology Series. California Institute of Technology, Pasadena (2009)
  28. Hershkowitz, N., Smith, J.R., Kozima, H.: Electrostatic self-plugging of a picket fence cusped magnetic field. *Phys. Fluids* **22**, 122–125 (1979). <https://doi.org/10.1063/1.862450>
  29. Leung, K.N., Hershkowitz, N., MacKenzie, K.R.: Plasma confinement by localized cusps. *Phys. Fluids* **19**, 1045–1053 (1976). <https://doi.org/10.1063/1.861575>
  30. Knorr, G., Merlino, R.L.: The role of fast electrons for the confinement of plasma by magnetic cusps. *Plasma Phys. Control. Fusion* **26**, 433–442 (1984). <https://doi.org/10.1088/0741-3335/26/2/004>
  31. Heidemann, R., Weis, S., Genovese, A., Lazurenko, A., Stalzer, H., Bosch, E., Holtmann, P.: Development of the low power HEMPT EV0. In: Paper Presented at the 36th International Electric Propulsion Conference, University of Vienna, Vienna, Austria, September 15–20 2019 (2019)
  32. Koch, N., Harmann, H., Kornfeld, G.: Status of the THALES high efficiency multi stage plasma thruster development for HEMP-T 3050 and HEMP-T 30250. In: Paper Presented at the 30th International Electric Propulsion Conference, Florence, Italy, September 17–20 2007 (2007)
  33. Young, C., Smith, A., Cappelli, M.: Preliminary characterization of a diverging cusped field (DCF) thruster. In: Paper Presented at the 31st International Electric Propulsion Conference, University of Michigan, Ann Arbor, Michigan, USA, September 20–24 2009 (2009)
  34. Hu, P., Liu, H., Gao, Y., Yu, D.: Effects of magnetic field strength in the discharge channel on the performance of a multi-cusped field thruster. *AIP Adv.* (2016). <https://doi.org/10.1063/1.4962548>
  35. Cui, K., Liu, H., Jiang, W.J., Sun, Q.Q., Hu, P., Yu, D.R.: Effects of cusped field thruster on the performance of drag-free control system. *Acta Astron.* **144**, 193–200 (2018). <https://doi.org/10.1016/j.actaastro.2017.12.032>
  36. Meeker, D.: *Finite element method magnetics: OctaveFEMM, Version 1.2. User's Manual* (2006)
  37. Conversano, R.W., Goebel, D.M., Hofer, R.R., Mikellides, I.G., Wirz, R.E.: Performance analysis of a low-power magnetically shielded hall thruster: experiments. *J. Propuls. Power* **33**, 975–983 (2017). <https://doi.org/10.2514/1.B36230>

**Publisher's Note** Springer Nature remains neutral with regard to jurisdictional claims in published maps and institutional affiliations.